Large spin-to-charge conversion in ultrathin gold-silicon multilayers

Mohammed Salah El Hadri*
Center for Memory and Recording Research, University of California San Diego, La Jolla, California 92093-0401, USA

Jonathan Gibbons
Department of Physics, University of California San Diego, La Jolla, California 92093-0401, USA;
Materials Science Division, Argonne National Laboratory, Argonne, Illinois 60439, USA;
and Department of Materials Science and Engineering and Materials Research Laboratory,
University of Illinois at Urbana-Champaign, Urbana, Illinois 61801, USA

Yuxuan Xiao
Center for Memory and Recording Research, University of California San Diego, La Jolla, California 92093-0401, USA

Haowen Ren
Center for Memory and Recording Research, University of California San Diego, La Jolla, California 92093-0401, USA

Hanu Arava
Northwestern-Argonne Institute of Science and Engineering (NAISE), Northwestern University, Evanston, Illinois 60208, USA
and Materials Science Division (MSD), Argonne National Laboratory, Argonne, Illinois 60439, USA

Yuzi Liu
Center of Nanoscale Materials, Argonne National Laboratory, Argonne, Illinois 60439, USA

Zhaowei Liu
Department of Electrical and Computer Engineering, University of California San Diego,
9500 Gilman Drive, La Jolla, California 92093-0407, USA
and Materials Science and Engineering Program, University of California San Diego,
9500 Gilman Drive, La Jolla, California 92093-0418, USA

Amanda Petford-Long
Northwestern-Argonne Institute of Science and Engineering (NAISE), Northwestern University, Evanston, Illinois 60208, USA
and Materials Science Division (MSD), Argonne National Laboratory, Argonne, Illinois 60439, USA

Axel Hoffmann
Materials Science Division, Argonne National Laboratory, Argonne, Illinois 60439, USA
and Department of Materials Science and Engineering and Materials Research Laboratory,
University of Illinois at Urbana-Champaign, Urbana, Illinois 61801, USA

Eric E. Fullerton
Center for Memory and Recording Research, University of California San Diego, La Jolla, California 92093-0401, USA
and Department of Electrical and Computer Engineering, University of California San Diego,
9500 Gilman Drive, La Jolla, California 92093-0407, USA

(Received 9 March 2021; accepted 8 June 2021; published 21 June 2021)

Investigation of the spin Hall effect in gold has triggered increasing interest over the past decade, since gold combines the properties of a large bulk spin-diffusion length and strong interfacial spin-orbit coupling. However, discrepancies between the values of the spin Hall angle of gold reported in the literature have brought into question the microscopic origin of the spin Hall effect in Au. Here, we investigate the thickness dependence of the effective spin-charge conversion efficiency in single Au films and ultrathin Au/Si multilayers by nonlocal transport and spin-torque ferromagnetic resonance measurements. We show that the inferred effective spin-charge conversion efficiency is strongly enhanced in ultrathin Au/Si multilayers, reaching exceedingly large values of 0.99 ± 0.34 when the thickness of the individual Au layers is scaled down to 2 nm. These findings reveal

*melhadri@ucsd.edu

the coexistence of a strong interfacial spin-to-charge conversion effect, which becomes dominant in ultrathin Au, and bulk spin Hall effect with a relatively low bulk spin Hall angle of 0.012 ± 0.005. Our experimental results suggest the key role of the intrinsic spin Hall effect enhancement along with a strong interfacial spin-orbit coupling-related effect in the large spin-to-charge conversion in ultrathin Au.

DOI: 10.1103/PhysRevMaterials.5.064410

I. INTRODUCTION

The interplay between spin-orbit coupling (SOC) and low dimensionality has attracted significant interest over the last decade due to the prospect of exploring rich physical mechanisms, as well as the potential impact on emerging spintronics technologies [1–4]. One of the most prominent mechanisms arising from the relativistic SOC is the spin Hall effect (SHE) [5,6]. This effect converts unpolarized charge currents into transverse spin currents, and vice versa, even in nonmagnetic conductors due to spin-orbit coupling [5]. The efficiency of the conversion of charge currents into spin currents via SHE is characterized by the spin Hall angle (SHA), which is defined as $\theta_{\mathrm{SHE}} = (2e/\hbar)(\sigma^s_{xy}/\sigma^c_{xx})$, where σ^s_{xy} and σ^c_{xx} are the spin Hall and charge conductivities, respectively, e is the electron charge, and $\hbar$ is the reduced Planck's constant [5]. The SHE is material-dependent and can be generated by both intrinsic and extrinsic mechanisms. The intrinsic mechanism relies on the strong intrinsic SOC in materials such as $4d$ and $5d$ transition metals [5]. On the other hand, the extrinsic mechanisms rely on scattering by impurities, and can be attributed to skew scattering [7] or side jump [8] mechanisms. Since its initial prediction by D'yakonov and Perel in 1971 [9], the spin Hall effect has attracted increasing interest from theoretical [10–12] and experimental [13–17] viewpoints, and has become an important tool for the injection, detection, and manipulation of spin currents in thin films and heterostructures [5,6,18–23].

The spin Hall effect can also be characterized by the spin-torque efficiency, which is defined in the case of nonmagnetic/magnetic heterostructures as J_S/J_C, where J_S is the spin current density absorbed by the magnetic layer and generated via SHE by the charge current density J_C in the nonmagnetic layer [24]. Note that for a perfectly transparent nonmagnetic/magnetic interface and for a nonmagnetic layer thickness much thicker than the spin-diffusion length, the spin-torque efficiency and θ_{SHE} should be equal [24]. Recent studies have explored new pathways to enhance the SHE by investigating novel chemically inhomogeneous [25–28] and multilayer [29,30] systems, and reported large spin-torque efficiencies, namely 0.35 for $Au_{1-x}Pt_x$ alloys [25], –0.49 for oxidized W [26], 0.9 for oxidized Pt [27,28], 0.37 for Pt/Hf multilayers [29], and 0.35 for Pt/Ti multilayers [30]. More importantly, the spin-torque efficiencies reported for these novel systems are much larger than the θ_{SHE} values reported for single-element layers, namely –0.33 for β-W [19], ∼0.1 for Pt [31,32], and 0.11 for Au [33], thus highlighting the importance of chemical inhomogeneity and heterostructures in the SHE mechanism. On the other hand, introducing low dimensionality to heavy metals with a large bulk SHE can also significantly enhance the spin-charge conversion efficiency via interfacial SOC-related effects, such as the Rashba SOC [34–37]. Hence, these emergent interfacial SOC phenomena offer promising routes for 2D-spintronics applications [1–3,38,39].

Since Au combines the properties of strong SOC at interfaces [33,40–42] and a relatively large bulk spin-diffusion length [43–45], it has been the focus of intense research interest, evidenced by many experimental and theoretical investigations. In 2008, Seki *et al.* reported a giant SHA of 0.11 in 10-nm-thick Au using an FePt perpendicular spin injector [33]. Later, nonlocal transport measurements by Mihajlović *et al.* showed the absence of the giant SHE in a 60-nm-thick H-shaped Au structure ($\theta_{\mathrm{SHE}} \leqslant 0.023$) [46], thus triggering a debate on the microscopic origin of the giant SHE in Au films. Follow up experimental investigations using various methods, such as nonlocal spin injection [47], spin pumping [48], and nonlocal transport [49,50], have revealed that the SHA of Au can be significantly reduced for films thicker than 10 nm. More recently, first-principles calculations demonstrated the presence of a strong interfacial contribution to the SHE in Au-Fe bilayers, which was attributed to spin-dependent transmission occurring within a few atomic layers [51]. More importantly, such an interfacial contribution occurs at the Au(111) interface where a strong Rashba SOC exists [40–42], which is a hint that the Rashba-splitting of the Au(111) surface states plays an important role in the spin-to-charge conversion mechanism in Au [51]. These investigations give insights into the origin of the large spin-to-charge conversion in Au and suggest the important role of the interface scattering [47,48,50] and/or the Rashba SOC [51].

To further elucidate the microscopic origin of the spin-to-charge conversion in Au films, we present an experimental investigation of the spin-to-charge conversion in ultrathin Au films and ultrathin Au/Si multilayers, where the thickness of the individual Au layers is scaled down to 2 nm. We utilized two different transport measurement techniques to probe the spin-to-charge conversion, nonlocal transport and spin-torque ferromagnetic resonance (ST-FMR), which probe the spin currents flow in the ultrathin Au layers in the in-plane and the out-of-plane directions, respectively (see Fig. 1). It would be more appropriate to characterize the spin-to-charge conversion in ultrathin Au by an effective spin-charge conversion efficiency (θ_{sc}), rather than by a bulk SHA (θ_{SHE}) [see Eq. (1)], since the spin-to-charge conversion probed in ultrathin Au can arise not only from bulk SHE, but also from interfacial SOC-related effects. In the case of a spin-to-charge conversion dominated by SHEs, θ_{sc} and θ_{SHE} should be equal. We demonstrate that the inferred θ_{sc} is strongly enhanced in ultrathin Au/Si multilayers, reaching values much larger than all SHA values previously reported for Au films [33,48,50]. Moreover, a similar thickness-dependent behavior of θ_{sc} was obtained using the ST-FMR technique, however, with much

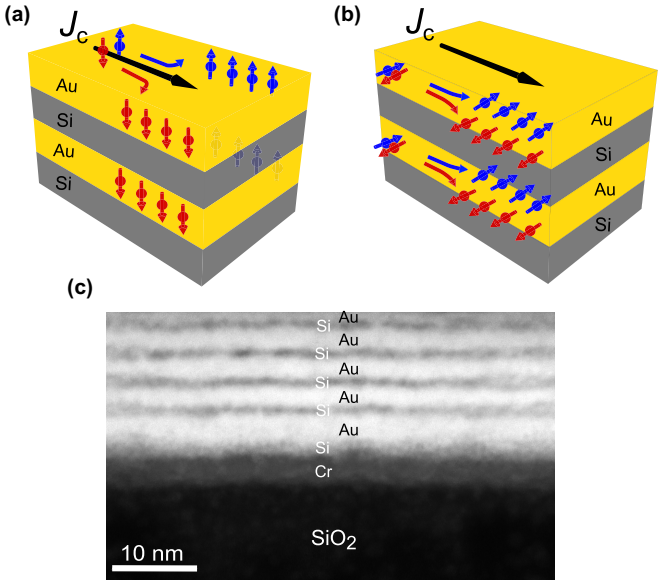

FIG. 1. [(a),(b)] Schematic representation of the spin Hall effect in ultrathin Au/Si multilayers showing the in- and out-of-plane spin currents, respectively. (c) Dark-field cross-sectional STEM image of [Si (1.8 nm)/Au (2 nm)]$_{x5}$ multilayer stack sputtered on a glass/Cr (3 nm), showing well-defined layered structure. The lighter regions correspond to the Au layers, while the dark regions correspond to the Si interlayers and the Cr buffer layer.

lower inferred θ_{sc} values. These findings indicate the coexistence of the bulk SHE with a relatively low bulk SHA and a strong interfacial SOC effect, which becomes dominant in ultrathin Au.

II. SAMPLE FABRICATION

We have chosen to study the spin-to-charge conversion in ultrathin Au/Si multilayers as they provide a unique opportunity to investigate the effective spin-charge conversion efficiency of Au averaged over many individual Au layers. Indeed, measuring the nonlocal transport in one ultrathin [Au (t_{Au})/Si (t_{Si})]$_N$ multilayer sample is equivalent to measuring N different single ultrathin Au (t_{Au}) layer samples, which would give more accuracy on the effective spin-charge conversion efficiency results. Moreover, it has been shown experimentally that Au/Si(111) interfaces can have metallic spin-split surface states with an energy splitting up to 190 meV, which at the same time is very sensitive to the local structure [52]. Furthermore, Au/Si multilayers present a very promising system that exhibits the properties of hyperbolic metamaterials (HMMs), which have recently emerged as one of the prime candidates for extraordinary manipulation of light [53,54]. In our nonlocal transport experiments, which probe the spin currents flow in the in-plane direction, as shown in Fig. 1(a), four different samples were investigated: two single polycrystalline Au films [Au (10 nm) and Au (60 nm)]; and two Au/Si multilayers [[Si (1.8 nm)/Au (2 nm)]$_{x5}$ and Au (5 nm)/[Si (4 nm)/Au (5 nm)]$_{x5}$]. Each sample was deposited on a glass/Cr (3 nm) substrate using a dc sputtering technique. The Cr buffer layer is used to ensure good adhesion of the single Au layers and the Au/Si multilayers to the substrate (see Methods within the Supplemental Material [55]). The thickness of the insulating Si interlayers is chosen to be sufficiently large ($t_{Si} \geqslant 1.5$ nm) to prevent strong coupling between the individual Au layers [56]. To verify the multilayer nature of the studied sample with the thinnest Si and Au layer thicknesses of 1.8 nm and 2 nm, we performed dark-field cross-sectional scanning transmission electron microscopy (STEM). Figure 1(c) shows the cross-sectional STEM view of the [Si (1.8 nm)/Au (2 nm)]$_{x5}$ multilayer structure, indicating a well-defined layered Au/Si structure and the absence of a strong cumulative roughness along the growth direction. The multilayer nature of the studied Au/Si films was also confirmed by x-ray reflectivity measurements, and with high-resolution transmission microscopy (HR-TEM) imaging on ultrathin Au/Si multilayers grown on a c-Si substrate (see Fig. S1 within the Supplemental Material [55]).

To further investigate the dependence of spin Hall properties on the direction of the spin currents, we also used the ST-FMR technique, which probes the spin currents that flow in the out-of-plane direction, as illustrated in Fig. 1(b). In our ST-FMR experiments, we investigated both single Au films and ultrathin Au/Si multilayers: three single polycrystalline Au (t_{Au}) films, where $t_{Au} = 2, 3, 5$ nm; and nine Au (t_{Au})/[Si (t_{Si})/Au (t_{Au})]$_{x4}$ multilayers, where $t_{Au} = 2, 3, 4$ nm and the thickness of the insulating Si interlayers $t_{Si} = 2, 3, 4$ nm. Each of these single Au films and Au/Si multilayers was sputter-deposited on a glass/Si (5 nm) substrate, and was capped with $Ni_{81}Fe_{19}$ (4 nm)/SiN_x (3 nm). The relatively low thickness of the $Ni_{81}Fe_{19}$ layer is chosen to ensure that the radio-frequency (RF) charge current flows evenly through the $Ni_{81}Fe_{19}$ and individual Au layers, while the 3-nm-thick SiN_x capping layer is used to prevent oxidation of the $Ni_{81}Fe_{19}$ layer (see Methods within the Supplemental Material [55]).

III. RESULTS

A. Nonlocal transport measurements

To probe the nonlocal transport, we patterned the four studied films into H-bar devices depicted in Fig. 2(a) using e-beam lithography and Ar ion-beam etching (see Methods within the Supplemental Material [55]). A top-view scanning electron microscope (SEM) image of the central region of such a H-bar device is shown in Fig. 2(b). The Hall bar device consists of six vertical wires of a width w separated by a center-to-center distance L and bridged by a horizontal wire of the same w. For the two Au/Si multilayers and the single Au (10 nm) samples, w is chosen to be 90 nm; this dimensionality is confirmed from SEM images, from which w is measured to be (90 ± 5) nm. On the other hand, the width w for the single Au (60 nm) sample is (110 ± 5) nm to be consistent with the previous study by Mihajlović *et al.* on the nonlocal transport in Au (60 nm) H-bar structures [46]. Moreover, the distance between the vertical wires L is varied from (180 ± 10) nm to (550 ± 10) nm for all studied samples. To perform the nonlocal transport measurements, an unpolarized ac current is injected along the left vertical wire (y axis) while a nonlocal voltage is measured in the adjacent wire (y direction). Three different transport mechanisms contribute to the nonlocal signal—the spin diffusive, the charge diffusive, and the

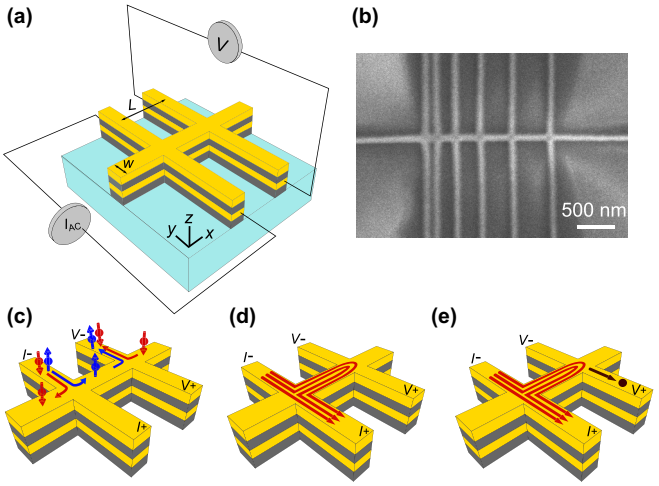

FIG. 2. (a) Experimental schematic of the nonlocal resistance measurement on Au/Si multilayers. (b) Top-view SEM image of the Si (1.8 nm)/Au (2 nm) multilayer film patterned into a H-bar device with six vertical 90-nm-wide wires separated by various distances and bridged by a horizontal one. [(c)–(e)] Schematic representation of the three mechanisms involved in the nonlocal transport in H-bar structures, namely the spin diffusive, the charge diffusive, and the quasi-ballistic transport, respectively.

quasi-ballistic-electron transport, as illustrated in Figs. 2(c)–2(e), respectively.

In the previous experimental studies utilizing nonlocal transport, the spin diffusive contribution to the nonlocal signal was interpreted solely in terms of the bulk SHE [46,49,50]. As shown in Fig. 2(c), the unpolarized charge current injected along the vertical wire induces a spin current in the horizontal wire due to the direct SHE. The spin current then diffuses and induces charge accumulation across the adjacent vertical wire via the inverse spin Hall effect (ISHE). Nevertheless, it was reported by Abanin *et al.* [57] that the spin diffusive contribution can result not only from the bulk SHE, but also from interfacial SOC-related effects such as the Edelstein effect and the Rashba SOC. Unlike for bulk SHE, the charge current in systems with strong 2D Rashba SOC induces a spin accumulation rather than a spin current, which creates a charge current in the adjacent wire via the inverse Edelstein effect. In our study, the spin diffusive contribution to the nonlocal transport in single Au layers and ultrathin Au/Si multilayers will be interpreted as originating from both the bulk SHE and interfacial SOC-related effects. Therefore, the spin-to-charge conversion in the studied H-bar structures is characterized by an effective spin-charge conversion efficiency θ_{sc}, rather than by a bulk SHA θ_{SHE}. According to the model by Abanin *et al.* [57], the spin diffusive contribution to the nonlocal resistance for $l_e \leqslant w$, where l_e is electron mean free path, is expressed by

$$R_{nl}^{sd} = \frac{1}{2} R_{sq} \theta_{sc}^2 \frac{w}{l_s} \exp\left(-\frac{L}{l_s}\right), \tag{1}$$

where l_s is the spin-diffusion length, θ_{sc} is the effective spin-charge conversion efficiency, and R_{sq} is the sheet resistance of the wire. In the case of [Au (t_{Au})/Si (t_{Si})]$_N$ multilayers where we assume that charge transport is negligible in Si, the sheet resistance equals $\frac{\rho_{Au}}{N t_{Au}}$, where ρ_{Au} is the resistivity of the individual Au layers, t_{Au} is the thickness of the individual Au layers, and N is the number of repeats.

In addition to the spin diffusive contribution, charge diffusion also contributes to the nonlocal signal when $l_e \leqslant w$. This corresponds to the spreading of the charge current density into the horizontal wire, leading to a nonzero voltage in the adjacent wire, as illustrated in Fig. 2(d). According to the van der Pauw theorem [58], the charge diffusion contribution for $L \geqslant w$ is defined as

$$R_{nl}^{cd} = R_{sq} \exp\left(-\pi \frac{L}{w}\right). \tag{2}$$

On the other hand, the electrons can also travel ballistically over the horizontal wire and then scatter ballistically into the lower region of the adjacent wire, thus generating a negative voltage as shown in Fig. 2(e). As described in Ref. [46], the quasi-ballistic contribution to the nonlocal signal can be expressed by

$$R_{nl}^{b} = -bR_{sq} \exp\left(-\frac{w}{l_e}\right) \exp\left(-\pi \frac{L}{w}\right), \tag{3}$$

where l_e is the electron mean free path and b is a fitting parameter. Hence, measuring a negative nonlocal resistance in the studied H-bar structures would be a signature of the quasi-ballistic transport mechanism [46]. To determine the sheet resistance R_{sq} of our four samples, we measured the local resistance R_{xx} as a function of temperature T for each segment of the horizontal wire between the adjacent vertical wires, as shown in the inset of Fig. 3(a). For both the local and nonlocal transport measurements, we present resistance values that are directly reported by a resistance bridge (AC Model 370 AC Resistance Bridge, LakeShore Cryotronics, Inc.). One can see from Fig. 3(a) that the local resistance R_{xx} increases linearly with the distance L at $T = 5$ K. Moreover, the linear fit of R_{xx} crosses the L axis in a finite distance L_0, indicating that the effective distance between each of the adjacent vertical wires corresponds to $L_{eff} = L - L_0$. This finding is in agreement with previous studies [46], and is attributed to the spreading of the charge current density into the vertical wires due to their finite width [46]. For the two Au/Si multilayers and the single Au (10 nm) layer samples, we measured an L_0 of (135 ± 5) nm [see Fig. 3(a) for Au (5 nm)/Si (4 nm) multilayers]. While for the single Au (60 nm) layer sample with $w = (110 \pm 5)$ nm, the measured L_0 is (83 ± 5) nm, which is in agreement with Ref. [46]. In the following, we will use $L = L_{eff}$ in Eq. (1)–(3).

To accurately estimate the resistivity of the Au layers ρ_{Au}, we first measured the resistivity of the 3-nm-thick Cr buffer layer ρ_{Cr} by performing temperature dependent resistance measurements on a glass/Cr (3 nm)/AlO_x (3 nm) sample. The AlO_x capping layer is used to prevent oxidation of the Cr layer. We found that the resistivity of the 3-nm-thick Cr layer decreases with increasing temperature from 250.1 $\mu\Omega$ cm at 5 K to 232.9 $\mu\Omega$ cm at 300 K. Therefore, the high resistivity of the 3-nm-thick Cr layer relative to that of Au indicates that most of the charge current flows through the Au layers, thus ruling out any strong contribution of the Cr layer to the nonlocal transport in the four investigated samples. Having considered the resistivity of the Cr buffer layer, we measured the temperature dependence of the resistivity of the individual

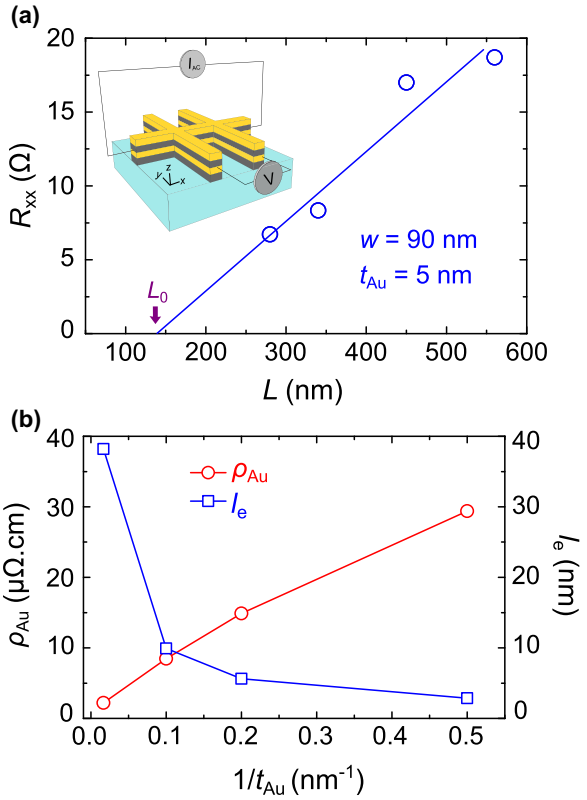

FIG. 3. (a) Resistance of each bridge wire between adjacent vertical wires of Au (5 nm)/Si (4 nm) multilayers as a function of L at $T = 5$ K. The blue solid line is a linear fit to the data. Upper inset: Experimental schematic of the local resistance measurement on Au/Si multilayers. (b) Resistivity ρ_{Au} and the corresponding electron mean free path l_e as a function of the inverse Au thickness $1/t_{Au}$ at 5 K, measured for the Au ($t_{Au} = 10$, 60 nm) films, as well as Au ($t_{Au} = 2$, 5 nm)/Si multilayers. The lines are guide to the eyes.

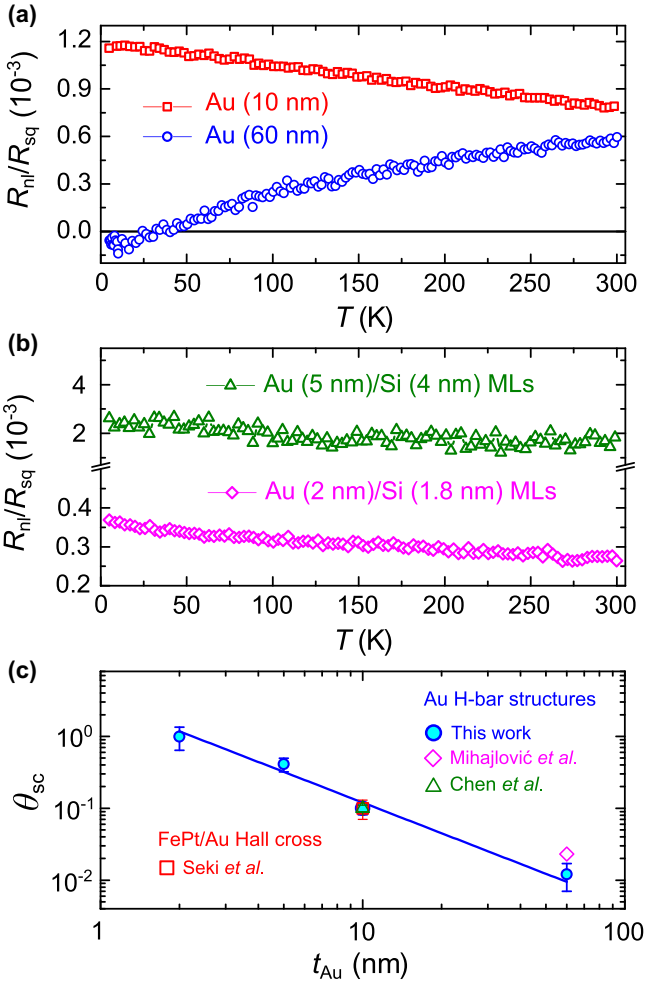

FIG. 4. (a) Temperature dependence of R_{nl}/R_{sq} measured for Au ($t_{Au} = 10$, 60 nm) films and for adjacent wires separated by a distance $L = 340$ nm. (b) Temperature dependence of R_{nl}/R_{sq} measured for Au ($t_{Au} = 5$ nm)/Si (4 nm) and Au ($t_{Au} = 2$ nm)/Si (1.8 nm) multilayers and for wires separated by a distance $L = 340$ nm and 450 nm, respectively. (c) Logarithmic plot of the effective spin-charge conversion efficiency θ_{sc} as a function of t_{Au} measured at $T = 5$ K for the single Au (t_{Au}= 10, 60 nm) films, as well as Au (t_{Au} = 5 nm)/Si (4 nm) and Au ($t_{Au} = 2$ nm)/Si (1.8 nm) multilayers. The blue solid line is a fit to the nonlocal transport data. For comparison, we also plot the θ_{SHE} values of Au from literature. Red square: Study of perpendicularly spin-polarized FePt/Au (10 nm) structure from Seki *et al.* [33]. Magenta diamond: Nonlocal transport in Au (60 nm) H-bar structure from Mihajlović *et al.* [46]. Green triangle: Nonlocal transport in Au (10 nm) H-bar structure from Chen *et al.* [50].

Au layers (ρ_{Au}) for the four studied samples. Figure 3(b) shows that the resistivity ρ_{Au} is inversely proportional to the thickness of the individual Au layers t_{Au}. Indeed, ρ_{Au} strongly increases from a bulk value of 2.2 $\mu\Omega$ cm (resp. 3.79 $\mu\Omega$ cm) at 5 K (resp. 300 K) for the single Au ($t_{Au} = 60$ nm) sample, to a much higher value of 29.4 $\mu\Omega$ cm (resp. 35.27 $\mu\Omega$ cm) at 5 K (resp. 300 K) for Au ($t_{Au} = 2$ nm)/Si (1.8 nm) multilayers. Such an increase in resistivity for ultrathin Au is in agreement with previous studies [48], and is mainly attributed to the dominance of surface scattering for ultrathin films. We further calculated the electron mean free path l_e values for the four studied samples using the Drude formula with an electron density for Au of $n = 5.9 \times 10^{28}$ m^{-3} [46]. We found that l_e strongly decreases from 38.2 nm (resp. 22.12 nm) at 5 K (resp. 300 K) for the single Au (60 nm) layer sample (in agreement with Ref. [46]) to 2.95 nm (resp. 2.48 nm) at 5 K (resp. 300 K) for Au ($t_{Au} = 2$ nm)/Si (1.8 nm) multilayers. These findings are attributed to the strong increase of ρ_{Au} in the ultrathin Au layers, and suggest that the quasi-ballistic contribution to the nonlocal resistance will be strongly suppressed in ultrathin Au-based multilayers.

We further measured the temperature dependence of the nonlocal resistance R_{nl} and extracted θ_{sc} for the four studied samples. Since all three different contributions to R_{nl} are proportional to the sheet resistance R_{sq}, we used the reduced nonlocal resistance R_{nl}/R_{sq} to investigate their temperature dependence. Figure 4(a) displays the T dependence of R_{nl}/R_{sq} measured for the single Au (60 nm) layer with $L = 340$ nm. One can see from Fig. 4(a) that R_{nl}/R_{sq} decreases when T is lowered and becomes negative around 33 K. This finding indicates that the nonlocal transport becomes dominated by the quasi-ballistic contribution at low temperatures in agreement with previous studies [46,50]. In order to extract θ_{sc} of the 60-nm-thick Au layer, we followed the method of Mihajlović

et al. [46] by plotting R_{nl}/R_{sq} as a function of l_e. As expected, we found that R_{nl}/R_{sq} fits with the quasi-ballistic and charge diffusive contributions to the nonlocal signal $(R_{nl}^{cd} + R_{nl}^{b})/R_{sq}$, where the fitting parameter $b = 22.14$ is used (see Fig. S2 within the Supplemental Material [55]). Thus, we deduced the T dependence of R_{nl}^{sd}/R_{sq} by subtracting $(R_{nl}^{cd} + R_{nl}^{b})/R_{sq}$ from R_{nl}/R_{sq}. By assuming the spin-diffusion length of Au l_s = 168 nm (resp. 65 nm) reported in Ref. [45] (resp. Ref. [44]), we extracted an upper limit for θ_{sc} of the Au (60 nm) sample of 0.012 (resp. 0.022) at 5 K, thus confirming the absence of a giant SHE in the studied Au (60 nm) sample. These inferred θ_{sc} values are consistent with the work by Mihajlović *et al.* [46] and, more importantly, confirm the absence of any contribution from the 3-nm-thick Cr buffer layer to the nonlocal transport.

In contrast to the single Au (60 nm) layer, R_{nl}/R_{sq} measured for the single Au (10 nm) layer with $L = 340$ nm is always positive and increases when T is lowered, as shown in Fig. 4(a). This finding is attributed to the increase of the resistivity ρ_{Au} in the Au (10 nm) layer, as shown in Fig. 3(b), leading to much lower l_e values ranging from 7.47 nm at 300 K to 9.92 nm at 5 K. Therefore, the contribution of $(R_{nl}^{cd} + R_{nl}^{b})/R_{sq}$ to R_{nl}/R_{sq} measured for the Au (10 nm) layer is not as dominant as for the Au (60 nm) layer, which explains the difference observed in the T dependence of R_{nl}/R_{sq} between these two samples. By assuming the b value of ~ 22.14, we found that $(R_{nl}^{cd} + R_{nl}^{b})/R_{sq}$ corresponds to 7.18×10^{-4} at 5 K for the Au (10 nm) layer. By subtracting $(R_{nl}^{cd} + R_{nl}^{b})/R_{sq}$ from R_{nl}/R_{sq}, we deduced a spin-diffusion contribution R_{nl}^{sd}/R_{sq} of 4.27×10^{-4}. To extract θ_{sc} of Au (10 nm), we assumed $l_s = (75 \pm 5)$ nm at 5 K, as demonstrated in a recent study on the nonlocal transport in Au (10 nm) [50]. From this, we extracted θ_{sc} of 0.1 ± 0.05 for the Au (10 nm) layer, which is in good agreement with other previous studies [33,49,50] as shown in Fig. 4(c). We now elucidate the nonlocal transport in the ultrathin Au/Si multilayers via the same approach previously used for the single Au layers. For Au ($t_{Au} \leqslant 5$ nm) layers, the electron mean free path l_e is drastically reduced ($l_e \leqslant 6$ nm) as previously discussed in Fig. 3(b). Hence, the quasi-ballistic contribution R_{nl}^{b}/R_{sq} will be strongly suppressed for the ultrathin Au/Si multilayers. Figure 4(b) shows that R_{nl}/R_{sq} measured for the Au ($t_{Au} \leqslant 5$ nm)/Si multilayers is always positive and increases when T is lowered, thus indicating that the nonlocal transport in these two multilayers is mostly dominated by the spin diffusion.

To extract θ_{sc} in these multilayers, we should first take into consideration the change of the spin-diffusion length with the increase of ρ_{Au} in the ultrathin Au. Indeed, it was previously reported in literature on materials with large l_s and spin relaxation via the Elliott-Yafet mechanism such as Au [45] and Cu [59], that l_s at low T decreases with the resistivity following the opposite trend of the thickness [45,59,60]. On the other hand, we measured a strong increase of ρ_{Au} at 5 K from the bulk value of 2.2 to 29.4 $\mu\Omega$ cm for 2-nm-thick Au. l_s is thus expected to be shorter for the ultrathin Au/Si multilayers. Therefore, it is reasonable to assume, for our estimation of a lower limit of θ_{sc}, that l_s corresponds to at most (43 ± 5) nm and (35 ± 5) nm at 5 K for each of the individual Au (5 nm) and Au (2 nm) layers, respectively. At $T = 5$ K, we extracted the following inferred values: θ_{sc} ($t_{Au} = 5$ nm) $= 0.41 \pm 0.09$ and θ_{sc} ($t_{Au} = 2$ nm) $= 0.99 \pm 0.34$, which are significantly larger than those extracted for the single Au ($t_{Au} = 10$, 60 nm) films. Furthermore, we extracted an inferred room-temperature (RT) θ_{sc} value of 0.87 ± 0.34 for Au (2 nm)/Si (1.8 nm) multilayers by assuming $l_s = (35 \pm 5)$ nm, which is exceedingly larger than bulk θ_{SHE} values reported for other heavy metals, such as –0.33 for β-W (from [19]), –0.12 for β-Ta (from [20]), and 0.1 for Pt (from [31,32]). This implies that these inferred effective spin-charge conversion efficiencies θ_{sc} cannot be interpreted solely in terms of the bulk SHE. By plotting the θ_{sc} values inferred for the four samples in a single graph on a logarithmic scale, one can see from Fig. 4(c) that θ_{sc} at $T = 5$ K is strongly enhanced for ultrathin Au thickness. This finding implies that the thickness and, therefore, the resistivity have a decisive effect on the spin-to-charge conversion in Au. More importantly, this strongly suggests the coexistence of a bulk SHE [$\theta_{SHE}^{bulk} \approx \theta_{sc}(t_{Au} = 60\ \text{nm}) = 0.012 \pm 0.005$] with a strong interfacial SOC effect, which becomes dominant in ultrathin Au. On the other hand, one can see that the θ_{sc} value of 0.1 ± 0.05 inferred for a single Au (10 nm) layer film is strongly enhanced when dicing the same Au layer into five individual 2-nm-thick Au layers (i.e., [Au (2 nm)/Si (1.8 nm)]$_{x5}$ multilayer) and reaches a large value of 0.99 ± 0.34. This finding highlights the role of dicing the same Au layer into several layers by inserting multiple ultrathin Si in enhancing the effective spin-charge conversion efficiency, in agreement with a recent study on Pt/Hf multilayers [29].

B. ST-FMR measurements

To give more insight into the microscopic origin of the spin-to-charge conversion in the ultrathin Au layers, it is important to elucidate the anisotropy of such a conversion with respect to the spin current flow direction. In this context, we further investigate the thickness-dependence of the spin-to-charge conversion in Au by using the ST-FMR technique, which probes the spin currents flow in the out-of-plane direction, as illustrated in Fig. 5(a). We studied both single Au (t_{Au})/$Ni_{81}Fe_{19}$ (4 nm) bilayers, where $t_{Au} = 2$, 3, 5 nm; and ultrathin Au (t_{Au})/[Si (t_{Si})/Au (t_{Au})]$_{x4}$/$Ni_{81}Fe_{19}$ (4 nm) multilayers, where $t_{Au} = 2$, 3, 4 nm and $t_{Si} = 2$, 3, 4 nm. The magnetization M of the 4-nm-thick $Ni_{81}Fe_{19}$ layer is oriented in-plane.

To probe the ST-FMR, we first patterned these studied films into 24-μm-wide and 88-μm-long microstrips using photolithography, and then fabricated symmetric waveguide contacts using dc sputtering and lift-off (see Methods within the Supplemental Material [55]). We applied an oscillating RF charge current I_{RF} at fixed frequencies f (7–9 GHz) along the microstrips, and swept an external magnetic field H in the in-plane direction at an angle $\varphi = 45^{\circ}$ with respect to the RF current direction, as illustrated in Fig. 5(a). An oscillating transverse spin current is then generated in each of the individual Au layers via the SHE. Hence, an oscillating spin-transfer torque induced by the out-of-plane spin current from the top Au layer is exerted on the $Ni_{81}Fe_{19}$ layer, leading to magnetization precession and an oscillation of the anisotropic magnetoresistance of $Ni_{81}Fe_{19}$. This anisotropic magnetoresistance transforms the magnetization precession in $Ni_{81}Fe_{19}$ into an RF resistance oscillation, which, by mixing

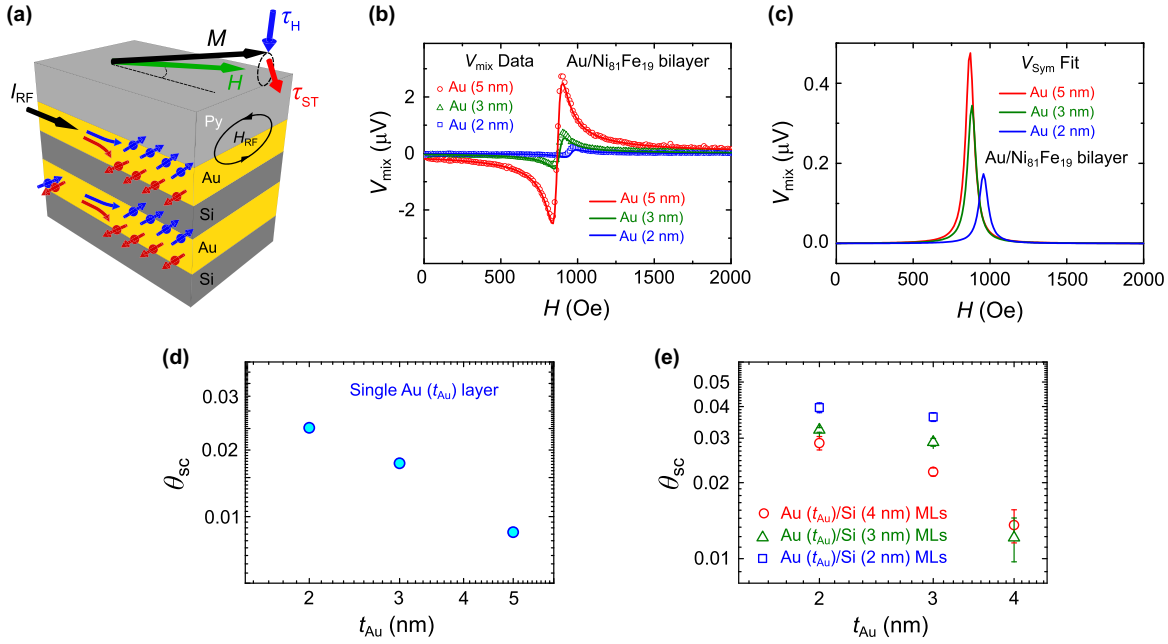

FIG. 5. ST-FMR measurement on single Au/$Ni_{81}Fe_{19}$ bilayers and ultrathin $[Si/Au]_N/Ni_{81}Fe_{19}$ multilayer stacks. (a) Schematic representation of the ST-FMR measurement in the ultrathin Au (t_{Au})/[Si (t_{Si})/Au (t_{Au})]$_{x4}$/$Ni_{81}Fe_{19}$ (4 nm) multilayer stack. I_{RF} and H_{RF} represent the applied radio frequency (RF) current and the corresponding Oersted field, respectively. The out-of-plane spin current generated via the SHE in the top ultrathin Au layer induces a spin-transfer torque τ_{ST} in the $Ni_{81}Fe_{19}$ layer. τ_H illustrates the torque induced by the Oersted field. H and M correspond to the external applied field and the magnetization of the $Ni_{81}Fe_{19}$ layer, respectively. $\varphi = 45^\circ$ is the angle between applied field H and the magnetization M. [(b),(c)] Representative ST-FMR resonance signals measured on Au (t_{Au})/$Ni_{81}Fe_{19}$ (4 nm) under a driving frequency $f = 8$ GHz and at room temperature, where $t_{Au} = 2$, 3 and 5 nm. The symbols in (b) represent the measured dc voltage V_{mix} data. The solid lines in (b) and (c) represent the antisymmetric and symmetric Lorentzian fitting curves, respectively, whose sum fits the measured V_{mix} data. (d) Logarithmic plot of θ_{sc} measured for single Au (t_{Au})/Pt (4 nm) bilayers as a function of t_{Au}, where $t_{Au} = 2$, 3, 5 nm. (e) Logarithmic plot of θ_{sc} measured for ultrathin Au (t_{Au})/[Si (t_{Si})/Au (t_{Au})]$_{x4}$/$Ni_{81}Fe_{19}$ (4 nm) multilayers as a function of t_{Au}, where $t_{Au} = 2$, 3, 4 nm and $t_{Si} = 2$, 3, 4 nm.

with the RF current, generates a measurable dc voltage signal V_{mix} across the sample. By varying the strength of the applied magnetic field H, the precession frequency of $Ni_{81}Fe_{19}$ is controlled, creating a resonance in V_{mix}. To extract the effective spin-charge conversion efficiency of Au, we then use a lineshape analysis of the measured V_{mix}. As described in Ref. [24], V_{mix} can be expressed by

$$V_{mix} = -\frac{1}{4}\frac{dR}{d\varphi}\frac{\gamma I_{RF}\cos\varphi}{\Delta 2\pi (df/dH)|_{H=H_0}}[SF_{Sym}(H) + AF_{Asym}(H)], \tag{4}$$

where $F_{Sym}(H) = \Delta^2/[\Delta^2 + (H - H_0)^2]$ is a symmetric Lorentzian centered at the resonant field H_0 with linewidth Δ, $F_{Asym} = F_{Sym}(H)(H - H_0)/\Delta$ is a antisymmetric Lorentzian, γ is the gyromagnetic ratio, R is the resistance of the microstrip, $\varphi = 45^\circ$ is the angle between applied field H and the magnetization M, and I_{RF} is the applied RF current. The symmetric component S is a consequence of the spin Hall antidamping torque induced by the out-of-plane spin current from the top Au layer. The antisymmetric component A arises from the field-like torques, expected to be dominated by the Oersted field H_{RF} from the RF current in each of the individual Au layers. The ST-FMR resonance signal V_{mix} measured on single Au (t_{Au})/$Ni_{81}Fe_{19}$ (4 nm) bilayers is exemplarily shown in Fig. 5(b). The corresponding antisymmetric and symmetric peaks are shown in Figs. 5(b) and 5(c), respectively.

We further quantitatively determined the θ_{sc} values in the studied samples by using the ratio of the symmetric component S to the antisymmetric component A. As described in Ref. [24], θ_{sc} of Au can be expressed by

$$\theta_{sc} = \frac{S}{A}\frac{e\mu_0 M_s t_{NiFe} N t_{Au}}{\hbar}\left(1 + \frac{4\pi M_{eff}}{H}\right)^{\frac{1}{2}}, \tag{5}$$

where μ_0 is the permeability in vacuum, M_s is the saturation magnetization of $Ni_{81}Fe_{19}$, M_{eff} is the effective magnetization of $Ni_{81}Fe_{19}$, which characterizes the out-of-plane demagnetization field, t_{NiFe} is the thickness of the $Ni_{81}Fe_{19}$ layer, t_{Au} is the thickness of the individual Au layers, N is the number of the individual Au layers, and H is the external magnetic field. For each of the studied samples, M_s is measured with vibrating sample magnetometry (VSM), while $4\pi M_{eff}$ is extracted by fitting the frequency dependence of the resonance field to the Kittel equation [24]. We found that the values M_s and M_{eff} are very similar, around 6.7×10^5 A/m, which is mainly due to the strong in-plane anisotropy of the $Ni_{81}Fe_{19}$ layer.

Figure 5(d) displays the Au thickness dependency of the room-temperature θ_{sc} values inferred for single Au (t_{Au})/$Ni_{81}Fe_{19}$ (4 nm) bilayers, where $t_{Au} = 2$, 3, 5 nm. One can see from Fig. 5(d) that θ_{sc} strongly increases from

8.5×10^{-3} to 0.025 when t_{Au} is scaled down from 5 to 2 nm, a trend that is consistent with the nonlocal transport results. Nevertheless, these inferred room-temperature θ_{sc} values obtained from the ST-FMR are much smaller than those extracted from the nonlocal transport at 5 K or 300 K. On the other hand, the inferred θ_{sc} values obtained from the ST-FMR do not account for the reduction of the spin transparency at the $Au/Ni_{81}Fe_{19}$ interface originating from the spin backflow (SBF) and the spin memory loss (SML) [61], which is thought to often reduce of the out-of-plane spin torques by at least a factor of two. By taking these effects into account, the effective spin-charge conversion efficiency for 2-nm-thick Au measured with ST-FMR is expected to be as large as 0.1, which is still one order of magnitude lower than the efficiency measured for 2-nm-thick Au with nonlocal transport. Hence, the effects of spin memory loss/spin backflow alone cannot explain the discrepancy between the effective spin-charge conversion efficiency values.

The discrepancy between the inferred θ_{sc} values might also suggest that the spin-to-charge conversion in ultrathin Au is anisotropic, favoring more efficient spin-to-charge conversion in the in-plane direction rather than the out-of-plane direction. Indeed, large anisotropies of the spin Hall conductivities are very plausible in multilayered samples, and that the nonlocal transport and ST-FMR measurements probe the spin currents flow in the in-plane and out-of-plane directions, respectively. Just as a comparison, theoretical first-principle calculations of SHEs in *hcp* elemental metals suggest anisotropies, even exceeding the ones observed in our measurements, for spin currents parallel or perpendicular to the basal plane [62]. This theoretical work predicted even the possibility of sign changes of SHA for the two different directions. Furthermore, anisotropies of spin Hall conductivities were also reported in previous experimental studies [63–66].

We further extracted the room-temperature θ_{sc} values in ultrathin Au (t_{Au})/[Si (t_{Si})/Au (t_{Au})]$_{x4}$/$Ni_{81}Fe_{19}$ (4 nm) multilayers, as shown in Fig. 5(e). Similar to the single $Au/Ni_{81}Fe_{19}$ bilayers, θ_{sc} increases from 0.012 to 0.039 by scaling down t_{Au} from 4 to 2 nm in ultrathin $[Si/Au]_N/Ni_{81}Fe_{19}$ multilayers. Note that these inferred θ_{sc} values are slightly larger than those obtained for single $Au/Ni_{81}Fe_{19}$ bilayers. This finding may be explained by the enhanced surface scattering in $[Si/Au]_N/Ni_{81}Fe_{19}$ multilayers due to the sample roughness, which enhances the extrinsic contribution to the SHE and, therefore, the θ_{sc} value.

IV. DISCUSSION

The sharp increase of the θ_{sc} in ultrathin Au, demonstrated by both nonlocal transport and ST-FMR techniques, calls into question the interpretation of the spin-to-charge conversion as originating solely from the bulk SHE, and suggests the coexistence of both bulk and interfacial mechanisms. To further elucidate the microscopic origin of the spin-to-charge conversion in Au, we discuss the thickness dependence of θ_{sc} by fully accounting for both intrinsic and extrinsic SHEs. Owing to the intrinsic SOC in the band structure, the intrinsic SHA in Au can be expressed by $\theta_{SHE}^{intrinsic} = \sigma_{SHE}^{intrinsic}/\sigma_{Au}$, where $\sigma_{SHE}^{intrinsic}$ is the intrinsic SHE conductivity and σ_{Au} is the longitudinal conductivity of Au. Such an intrinsic contribution

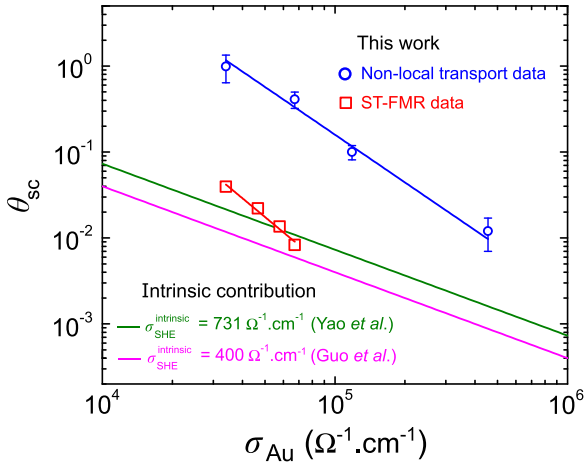

FIG. 6. Logarithmic plot of the effective spin-charge conversion efficiency θ_{sc} as a function of the longitudinal conductivity σ_{Au} of Au for the samples investigated in this work with nonlocal transport and ST-FMR measurements. The blue and red solid lines are a fit to the nonlocal transport and ST-FMR data, respectively. The green and magenta solid lines correspond to the intrinsic contribution to the SHA in Au $\theta_{SHE}^{intrinsic} = \sigma_{SHE}^{intrinsic}/\sigma_{Au}$ using $\sigma_{SHE}^{intrinsic} = 400\ \Omega^{-1}\ cm^{-1}$ from Guo *et al.* [69] and $\sigma_{SHE}^{intrinsic} = 731\ \Omega^{-1}\ cm^{-1}$ from Yao *et al.* [70].

can be the dominant mechanism in a moderately dirty metal, as reported in an experimental study on Pt by Sagasta *et al.* [67]. Since scaling down the Au thickness to a few nm is accompanied by a strong increase of the resistivity ρ_{Au}, one may intuitively attribute the strong enhancement of θ_{sc} in ultrathin Au to the intrinsic SHE mechanism. Nevertheless, the intrinsic SHE conductivity of Au is relatively small due to the small *d*-electron density of states at the Fermi level, in contrast to that of Pt [68]. Indeed, theoretical studies on Au have predicted relatively small $\sigma_{SHE}^{intrinsic}$ values, namely $400\ \Omega^{-1}\ cm^{-1}$ [69] and $731\ \Omega^{-1}\ cm^{-1}$ [70]. To verify the role of the intrinsic SHE in Au, we plot in Fig. 6 the inferred θ_{sc} values and the theoretically predicted $\sigma_{SHE}^{intrinsic}$ as a function of σ_{Au} on a logarithmic scale. Despite the discrepancy between the θ_{sc} values inferred from the nonlocal transport and ST-FMR measurements, one can see from Fig. 6 that logarithmic slopes of θ_{sc} for both techniques are very similar. Moreover, Fig. 6 shows that $\theta_{SHE}^{intrinsic}$ increases in ultrathin Au with low σ_{Au} values, with a logarithmic slope smaller than the one of the inferred θ_{sc}. More importantly, the predicted $\theta_{SHE}^{intrinsic}$ values in ultrathin Au are still smaller than the θ_{sc} values inferred from the nonlocal transport measurements as well as the SHA values reported in previous studies [33,46,50]. Therefore, the intrinsic SHE contribution alone cannot explain the strong increase of θ_{sc} in ultrathin Au.

The strong increase of θ_{sc} is also unlikely to be explained by the extrinsic skew scattering SHE, since this extrinsic contribution is dominant only for clean metals [5] and should decrease in the relatively highly resistive ultrathin Au. Nevertheless, previous experimental and theoretical studies on the SHE in Au using perpendicularly spin-polarized FePt/Au structures revealed the key role of the extrinsic skew scattering contribution [33,47,71,72]. Indeed, it was reported that the

large SHA of ∼0.11 measured in FePt/Au (10 nm) structure originates from the extrinsic surface-assisted skew scattering due to Pt impurities [33,47,71] and/or Fe Kondo impurities [72]. However, we measured a similar θ_{sc} value in Au (10 nm) H-bar structures with the nonlocal transport, in agreement with Ref. [50], where both magnetic and strong SOC impurities are absent. This finding rules out the interpretation that the strong increase of θ_{sc} in ultrathin Au layers arises from the previously reported surface-assisted skew scattering mechanism [33,47,71,72]. Furthermore, it was shown in a recent theoretical study that the surface scattering combined with a strong interfacial SOC can lead to a SHE that subscribes only to the extrinsic side-jump SHE, which is usually dominant for moderately dirty metals [73]. Hence, this extrinsic contribution could explain the thickness-dependence of θ_{sc} in Au; however, it is unlikely to explain the large θ_{sc} values inferred in ultrathin Au from the nonlocal transport measurements.

The inverse proportionality between the effective spin-charge conversion efficiency and the Au layer thickness strongly suggest that the enhancement arises from an interfacial SOC phenomena, such as the Rashba-Edelstein effect. On the other hand, previous angle-resolved photoemission spectroscopy (ARPES) studies revealed a large Rashba-type splitting on Au(111) surface [40–42], indicating the presence of a strong interfacial Rashba SOC. More importantly, it has been shown in a previous experimental study by Bondarenko *et al.* that the Au/Si(111) interface can have metallic spin-split surface states with a large spin-splitting energy of 190 meV [52]. In our sputter-deposited ultrathin Au/Si multilayers, the interfacial Rashba SOC effect might be strongly reduced in the multilayer stacking due to the opposite directional Rashba SOC in opposite interfaces. Note that the opposite interfaces in low/high Z element-multilayers such as Au/Si multilayers might be not equivalent, as it was previously demonstrated on Nb/Si multilayers [74]. Hence, one would expect that the Rashba-Edelstein contributions from the opposite interfaces in our sputter-deposited Au/Si multilayers would not completely cancel out. Moreover, the interfacial Rashba SOC effect will survive in the topmost layer where a strong (111) out-of-plane texture interface was evidenced by HR-TEM imaging (see Fig. S1 within the Supplemental Material [55]), in agreement with Ref. [75]. The spin-splitting energy at the Au/Si(111) interface is as large as the one reported for the Bi/Ag(111) interface, i.e., 200 meV [76]. Moreover, Rojas-Sánchez *et al.* experimentally demonstrated a large spin-to-charge conversion at the Bi/Ag Rashba interface [38], which yields a SHA of 1.5 when interpreted only by the bulk SHE. Taking these findings into account, the increase of the inferred θ_{sc} in ultrathin Au to exceptionally large values (∼0.99 for $t_{Au} = 2$ nm) can be plausibly explained by the Edelstein effect, arising from the strong interfacial Rashba SOC. Nevertheless, the contribution of the intrinsic SHE to enhancement of the effective spin-charge conversion efficiency in ultrathin Au cannot be completely excluded based on our findings in Fig. 6.

V. CONCLUSIONS

In conclusion, we have experimentally investigated the thickness dependence of the effective spin-charge conversion efficiency θ_{sc} in single Au films and ultrathin Au/Si multilayers with two different techniques, namely nonlocal transport and ST-FMR. We first found that the θ_{sc} values measured for the single Au ($t_{Au} = 10$, 60 nm) layers are consistent with the literature. Moreover, we demonstrated that θ_{sc} of Au measured with the nonlocal transport in ultrathin Au ($t_{Au} = 2$, 5 nm)/Si multilayers is strongly enhanced and reaches exceedingly large inferred values. A similar thickness-dependent behavior of θ_{sc} was obtained using the ST-FMR technique, however, with much lower inferred θ_{sc} values. Our experimental results evidence the coexistence of a strong interfacial spin-to-charge conversion effect, which becomes dominant in ultrathin Au, and bulk SHE with a relatively low bulk SHA. More importantly, these findings would suggest the key role of the intrinsic spin Hall effect enhancement along with a strong interfacial spin-orbit coupling-related effect in enhancing the spin-to-charge conversion in ultrathin Au, and help pave the way for the use of ultrathin Au in emerging spintronic devices.

ACKNOWLEDGMENTS

The authors would like to thank A. Fert, G. Mihajlović, M. Stiles, V. P. Amin, and F. Casanova for fruitful discussions, and R. Descoteaux from CMRR for technical assistance. The sample preparation was supported by the National Science Foundation under Grant No. NSF-DMR-1610538. The sample characterization, measurements, and data analysis were supported as part of Quantum Materials for Energy Efficient Neuromorphic Computing, an Energy Frontier Research Center funded by the US DOE, Office of Science under Award No. DE-SC0019273.

The authors declare no competing financial interests.

[1] F. Hellman, A. Hoffmann, Y. Tserkovnyak, G. S. D. Beach, E. E. Fullerton, C. Leighton, A. H. MacDonald, D. C. Ralph, D. A. Arena, H. A. Dürr, P. Fischer, J. Grollier, J. P. Heremans, T. Jungwirth, A. V. Kimel, B. Koopmans, I. N. Krivorotov, S. J. May, A. K. Petford-Long, J. M. Rondinelli *et al.*, Rev. Mod. Phys. **89**, 025006 (2017).

[2] A. Soumyanarayanan, N. Reyren, A. Fert, and C. Panagopoulos, Nature (London) **539**, 509 (2016).

[3] A. Manchon, H. C. Koo, J. Nitta, S. M. Frolov, and R. A. Duine, Nat. Mater. **14**, 871 (2015).

[4] J. Sklenar, W. Zhang, M. B. Jungfleisch, W. Wiang, H. Saglam, J. E. Pearson, J. B. Ketterson, and A. Hoffmann, J. Appl. Phys. **120**, 180901 (2016).

[5] A. Hoffmann, IEEE Trans. Magn. **49**, 5172 (2013).

[6] J. Sinova, S. O. Valenzuela, J. Wunderlich, C. H. Back, and T. Jungwirth, Rev. Mod. Phys. **87**, 1213 (2015).

[7] J. Smit, Physica (Amsterdam) **24**, 39 (1958).

[8] L. Berger, Phys. Rev. B **2**, 4559 (1970).

[9] M. I. D'yakonov and V. I. Perel', Pis'ma Zh. Éksp. Teor. Fiz. **13**, 657 (1971) [JETP Lett. **13**, 467 (1971)].

[10] J. E. Hirsch, Phys. Rev. Lett. **83**, 1834 (1999).
[11] S. Zhang, Phys. Rev. Lett. **85**, 393 (2000).
[12] J. Sinova, D. Culcer, Q. Niu, N. A. Sinitsyn, T. Jungwirth, and A. H. MacDonald, Phys. Rev. Lett. **92**, 126603 (2004).
[13] S. O. Valenzuela and M. Tinkham, Nature (London) **442**, 176 (2006).
[14] Y. K. Kato, R. C. Myers, A. C. Gossard, and D. D. Awschalom, Science **306**, 1910 (2004).
[15] J. Wunderlich, B. Kaestner, J. Sinova, and T. Jungwirth, Phys. Rev. Lett. **94**, 047204 (2005).
[16] E. Saitoh, M. Ueda, H. Miyajima, and G. Tatara, Appl. Phys. Lett. **88**, 182509 (2006).
[17] T. Kimura, Y. Otani, T. Sato, S. Takahashi, and S. Maekawa, Phys. Rev. Lett. **98**, 156601 (2007).
[18] Q. Shao, P. Li, L. Liu, H. Yang, S. Fukami, A. Razavi, H. Wu, K. L. Wang, F. Freimuth, Y. Mokrousov *et al.*, IEEE Trans. Magn. (2021), doi:10.1109/TMAG.2021.3078583.
[19] C.-F. Pai, L. Liu, H. W. Tseng, D. C. Ralph, and R. A. Buhrman, Appl. Phys. Lett. **101**, 122404 (2012).
[20] L. Liu, C.-F. Pai, Y. Li, H. W. Tseng, D. C. Ralph, and R. A. Buhrman, Science **336**, 555 (2012).
[21] L. Liu, O. J. Lee, T. J. Gudmundsen, D. C. Ralph, and R. A. Buhrman, Phys. Rev. Lett. **109**, 096602 (2012).
[22] L. Liu, C.-F. Pai, D. C. Ralph, and R. A. Buhrman, Phys. Rev. Lett. **109**, 186602 (2012).
[23] A. Manchon, J. Železný, I. M. Miron, T. Jungwirth, J. Sinova, A. Thiaville, K. Garello, and P. Gambardella, Rev. Mod. Phys. **91**, 035004 (2019).
[24] L. Liu, T. Moriyama, D. C. Ralph, and R. A. Buhrman, Phys. Rev. Lett. **106**, 036601 (2011).
[25] L. Zhu, D. C. Ralph, and R. A. Buhrman, Phys. Rev. Appl. **10**, 031001(R) (2018).
[26] K.-U. Demasius, T. Phung, W. Zhang, B. P. Hughes, S.-H. Yang, A. Kellock, W. Han, A. Pushp, and S. S. P. Parkin, Nat. Commun. **7**, 10644 (2016).
[27] H. An, Y. Kanno, A. Asami, and K. Ando, Phys. Rev. B **98**, 014401 (2018).
[28] H. An, T. Ohno,Y. Kanno, Y. Kageyama, Y. Monnai, H. Maki, J. Shi, and K. Ando, Sci. Adv. **4**, eaar2250 (2018).
[29] L. Zhu, L. Zhu, S. Shi, M. Sui, D. C. Ralph, and R. A. Buhrman, Phys. Rev. Appl. **11**, 061004(R) (2019).
[30] L. Zhu and R. A. Buhrman, Phys. Rev. Applied **12**, 051002(R) (2019).
[31] M. Althammer, S. Meyer, H. Nakayama, M. Schreier, S. Altmannshofer, M. Weiler, H. Huebl, S. Geprägs, M. Opel, R. Gross, D. Meier, C. Klewe, T. Kuschel, J.-M. Schmalhorst, G. Reiss, L. Shen, A. Gupta, Y.-T. Chen, G. E. W. Bauer, E. Saitoh *et al.*, Phys. Rev. B **87**, 224401 (2013).
[32] W. Zhang, V. Vlaminck, J. E. Pearson, R. Divan, S. D. Bader, and A. Hoffmann, Appl. Phys. Lett. **103**, 242412 (2013).
[33] T. Seki, Y. Hasegawa, S. Mitani, S. Takahashi, H. Imamura, S. Maekawa, J. Nitta, and K. Takanashi, Nat. Mater. **7**, 125 (2008).
[34] E. I. Rashba, Fiz. Tverd. Tela **2**, 1224 (1960) [Sov. Phys. Solid State **2**, 1109 (1960)].
[35] M. Edelstein, Solid State Commun. **73**, 233 (1990).
[36] Yu. A. Bychkov and E. I. Rasbha, Pis'ma Zh. Eksp. Teor. Fiz. **39**, 66 (1984) [JETP Lett. **39**, 78 (1984)].
[37] A. A. Burkov, A. S. Núñez, and A. H. MacDonald, Phys. Rev. B **70**, 155308 (2004).
[38] J. C. Rojas-Sánchez, L. Vila, G. Desfonds, S. Gambarelli, J. P. Attane, J. M. De Teresa, C. Magen, and A. Fert, Nat. Commun. **4**, 2944 (2013).
[39] M. B. Jungfleisch, W. Zhang, J. Sklenar, W. Jiang, J. E. Pearson, J. B. Ketterson, and A. Hoffmann, Phys. Rev. B **93**, 224419 (2016).
[40] S. LaShell, B. A. McDougall, and E. Jensen, Phys. Rev. Lett. **77**, 3419 (1996).
[41] G. Nicolay, F. Reinert, S. Hüfner, and P. Blaha, Phys. Rev. B **65**, 033407 (2001).
[42] I. A. Nechaev, M. F. Jensen, E. D. L. Rienks, V. M. Silkin, P. M. Echenique, E. V. Chulkov, and Ph. Hofmann, Phys. Rev. B **80**, 113402 (2009).
[43] M. Johnson, Phys. Rev. Lett. **70**, 2142 (1993).
[44] Y. Ji, A. Hoffmann, J. S. Jiang, and S. D. Bader, Appl. Phys. Lett. **85**, 6218 (2004).
[45] J.-H. Ku, J. Chang, H. Kim, and J. Eom, Appl. Phys. Lett. **88**, 172510 (2006).
[46] G. Mihajlović, J. E. Pearson, M. A. Garcia, S. D. Bader, and A. Hoffmann, Phys. Rev. Lett. **103**, 166601 (2009).
[47] T. Seki, I. Sugai, Y. Hasegawa, and K. Takanashi, Solid State Commun. **150**, 496 (2010).
[48] J. T. Brangham, K.-Y. Meng, A. S. Yang, J. C. Gallagher, B. D. Esser, S. P. White, S. Yu, D. W. McComb, P. C. Hammel, and F. Yang, Phys. Rev. B **94**, 054418 (2016).
[49] D. Tian, C. Chen, H. Wang, and X. Jin, Chin. Phys. B **25**, 107201 (2016).
[50] C. Chen, D. Tian, H. Zhou, D. Hou, and X. Jin, Phys. Rev. Lett. **122**, 016804 (2019).
[51] S. Li, K. Shen, and K. Xia, Phys. Rev. B **99**, 134427 (2019).
[52] L. V. Bondarenko, D. V. Gruznev, A. A. Yakovlev, A. Y. Tupchaya, D. Usachov, O. Vilkov, A. Fedorov, D. V. Vyalikh, S. V. Eremeev, E. V. Chulkov, A. V. Zotov, and A. A. Saranin, Sci. Rep. **3**, 1826 (2013).
[53] H. Shen, D. Lu, B. VanSaders, J. J. Kan, H. Xu, E. E. Fullerton, and Z. Liu, Phys. Rev. X **5**, 021021 (2015).
[54] H. Qian, M. S. El Hadri, X. Wu, L. Chen, E. E. Fullerton, and Z. Liu (unpublished).
[55] See Supplemental Material at http://link.aps.org/supplemental/10.1103/PhysRevMaterials.5.064410 for methods, high-resolution transmission electron microscopy image of ultrathin Au/Si multilayers, and fitting of the nonlocal resistance measured for 60-nm-thick Au film.
[56] N. Cherradi, A. Audouard, G. Marchal, J. M. Broto, and A. Fert, Phys. Rev. B **39**, 7424 (1989).
[57] D. A. Abanin, A. V. Shytov, L. S. Levitov, and B. I. Halperin, Phys. Rev. B **79**, 035304 (2009).
[58] L. J. van der Pauw, Philips Tech. Rev. **20**, 220 (1958).
[59] E. Villamor, M. Isasa, L. E. Hueso, and F. Casanova, Phys. Rev. B **87**, 094417 (2013).
[60] M. Isasa, E. Villamor, L. E. Hueso, M. Gradhand, and F. Casanova, Phys. Rev. B **91**, 024402 (2015).
[61] C.-F. Pai, Y. Ou, L. H. Vilela-Leão, D. C. Ralph, and R. A. Buhrman, Phys. Rev. B **92**, 064426 (2015).
[62] F. Freimuth, S. Blugel, and Y. Mokrousov, Phys. Rev. Lett. **105**, 246602 (2010).
[63] V. Sih, R. C. Myers, Y. K. Kato, W. H. Lau, A. C. Gossard, and D. D. Awschalom, Nat. Phys. **1**, 31 (2005).

[64] W. Zhang, W. Han, S.-H. Yang, Y. Sun, Y. Zhang, B. Yan, and S. S. P. Parkin, Sci. Adv. **2**, e1600759 (2016).
[65] T. Nan *et al.*, PNAS USA **116**, 16186 (2019).
[66] R. Thompson, J. Ryu, G. Choi, S. Karube, M. Kohda, J. Nitta, and B.-G. Park, Phys. Rev Appl. **15**, 014055 (2021).
[67] E. Sagasta, Y. Omori, M. Isasa, M. Gradhand, L. E. Hueso, Y. Niimi, Y. C. Otani, and F. Casanova, Phys. Rev. B **94**, 060412(R) (2016).
[68] T. Tanaka, H. Kontani, M. Naito, T. Naito, D. S. Hirashima, K. Yamada, and J. Inoue, Phys. Rev. B **77**, 165117 (2008).
[69] G. Y. Guo, J. Appl. Phys. **105**, 07C701 (2009).
[70] Y. Yao and Z. Fang, Phys. Rev. Lett. **95**, 156601 (2005).
[71] B. Gu, I. Sugai, T. Ziman, G. Y. Guo, N. Nagaosa, T. Seki, K. Takanashi, and S. Maekawa, Phys. Rev. Lett. **105**, 216401 (2010).
[72] G.-Y. Guo, S. Maekawa, and N. Nagaosa, Phys. Rev. Lett. **102**, 036401 (2009).
[73] L. Zhou, V. L. Grigoryan, S. Maekawa, X. Wang, and J. Xiao, Phys. Rev. B **91**, 045407 (2015).
[74] E. E. Fullerton, J. Pearson, C. H. Sowers, S. D. Bader, X. Z. Wu, and S. K. Sinha, Phys. Rev. B **48**, 17432 (1993).
[75] J. J. Kan, Ph.D. thesis, University of California San Diego, 2014.
[76] C. R. Ast, J. Henk, A. Ernst, L. Moreschini, M. C. Falub, D. Pacilé, P. Bruno, K. Kern, and M. Grioni, Phys. Rev. Lett. **98**, 186807 (2007).